Climate Variability in a Coupled Atmosphere-Ocean Model: the Role of Ocean Mixed Layer Processes

Michael A. Alexander*
James D. Scott
NOAA-CIRES/Climate Diagnostics Center
University of Colorado

Clara Deser
National Center for Atmospheric Research

(Submitted to the Journal of Geophysical Research: Oceans)
March 1999

*Corresponding author address:
Dr. Michael Alexander
NOAA-CIRES/Climate Diagnostics Center
R/E/CD1
325 Broadway
Boulder, CO 80303-3328

ABSTRACT

A 50-year coupled atmosphere-ocean model integration is used to study sea surface temperature (SST) and mixed layer depth (*h*), and the processes which influence them. The model consists of an atmospheric general circulation model coupled to an ocean mixed layer model in ice-free regions. The midlatitude SST variability is simulated fairly well, although the maximum variance is underestimated and located farther south than observed. The model is clearly deficient in the vicinity of the Gulf Stream and in the eastern tropical Pacific where advective processes are important. The model generally reproduces the observed structure of the mean *h* in both March and September but underestimates it in the North Atlantic during winter.

The net surface heat flux strongly regulates both the mean ($\overline{\ }$)and anomalous (‘) SSTs throughout the year. The entrainment heat flux, which is proportional to the product of the entrainment rate (W_e) and the temperature jump at the base of the mixed layer (ΔT), influences SSTs in summer and fall, especially north of ~35˚N (45˚N) in the Pacific (Atlantic). $\overline{W_e}\Delta T'$ is more important for the development of (SST') in fall compared to $W_e'\overline{\Delta T}$, which is larger in summer. Anomalies in *h* have a significant impact on the heat balance of the mixed layer during spring and summer. The entrainment rate is dominated by wind-induced mixing in summer and surface buoyancy forcing in winter; the density jump at the base of the mixed layer is of secondary importance.

1. Introduction

Beginning with the pioneering work of Namias [1959, 1963] and Bjerknes [1964], numerous studies have sought to understand how midlatitude sea surface temperature (SST) anomalies form and the extent to which they influence the atmosphere. SST anomalies may form through changes in air-sea heat fluxes, horizontal and vertical ocean heat transport, and turbulent mixing. Many of the early studies [see Frankignoul, 1985], focused on the role of advection: Namias [1959, 1965] found that anomalous Ekman drift played an important role in generating SST anomalies, while Jacob(1967), Namias [1972], and Favorite and McClain [1973] suggested that the mean advection of anomalous temperatures could also be important. More recent modeling studies confirmed that anomalous Ekman transport could help to create SST anomalies in regions of strong SST gradients [Haney, 1980; Luksch and von Storch, 1992; Miller et al., 1994; Luksch, 1996]. However, on times scales of less than ~10 years, most studies have found that surface heat fluxes play a dominant role in forcing midlatitude SST anomalies [Gill and Niiler, 1973; Salmon and Hendershott, 1976; Frankignoul and Reynolds, 1983; Battisti et al., 1995; Halliwell and Mayer, 1996; plus many more], while Ekman pumping plays a negligible role [White et al., 1980; Haney et al., 1983; Schneider et al., 1999].

High resolution measurements of currents, temperature, and salinity indicate that upper ocean processes, in addition to surface heat fluxes, can have an important impact on SSTs [e.g. Davis et al., 1981; Large et al., 1986; Webster and Lukas, 1992]. However, most field studies are of short duration, generally lasting less than a few months. Longer records, on the order of 20-40 years, are available from a few of the ocean weather ships stationed in the North Atlantic and Pacific Oceans. Using weather ship data, Clark [1972], Elsberry and Garwood [1980], and Lanzante and Harnack [1983] found that the anomalies in the depth of the well mixed surface layer could significantly influence SSTs in spring and summer. Camp and Elsberry [1978] showed that cooling due to entrainment of subsurface water into the mixed layer could be an order of magnitude larger than the surface energy fluxes during the passage of storms at weather ship P (50˚N, 145˚W). Namias and Born [1970, 1974] and Alexander and Deser [1995] presented evidence that thermal anomalies created in the deep ocean mixed layer could remain intact in the seasonal thermocline (30-100 m) during summer and return to the surface layer in the following fall and winter. However, many upper ocean processes, such as entrainment, and their impact on SST are very difficult to measure directly.

Both bulk mixed layer models and layered models have been used to simulate vertical processes in the upper ocean [e.g. Garwood, 1977; Niiler and Kraus, 1977; Price et al,. 1986; Kantha and Clayson, 1994; Large et al., 1994]. In bulk models, the temperature (and salinity and currents if included) is predicted for the mixed layer as a whole, and the mixed layer depth (h) depends on processes which create turbulence including mechanical mixing by wind stress and convective mixing by the surface buoyancy flux. Bulk models appear to be as accurate in their simulation of SST and h as more sophisticated and computationally intensive layered models [Martin, 1985; Gaspar et al., 1988; Kraus, 1988]. However, both types of models have generally been developed and tested at a few weather ship locations, and bulk models can not reproduce the detailed vertical structure of turbulence. Bulk models have been used to study the mean seasonal cycle of SST and h [Gordon and Bottomly, 1985; Le Treut et al., 1985; Siminot et al., 1988] and the formation of SST anomalies over the North Pacific [Miyakoda and Roasatti, 1984; Alexander, 1992] and North Atlantic [Battisti et al., 1995].

Ocean mixed layer models are also useful for understanding the processes which contribute to the variability of SST and h over the course of the seasonal cycle. Alexander and Penland [1996] used a statistical atmospheric model, based on observations from weather ship P, to drive a mixed layer ocean model. The model provided a reasonable estimate of the range of the mean and standard deviation of upper ocean temperature and mixed layer depth over the seasonal cycle. An analysis of the temperature tendency indicated that anomalies in the net heat flux, mixed layer depth and entrainment heat flux all provided a significant contribution to the growth of SST anomalies at different times of the year. Anomalies in h were highly correlated with the surface buoyancy flux in winter and the surface wind stress in summer.

In this study, we expand on the work of Alexander and Penland [1996] by examining SST and h and the processes which influence them over the Northern Hemisphere Oceans in a coupled atmosphere-ocean model. The model, which consists of an atmospheric general circulation model (AGCM) connected to a grid of one-dimensional mixed layer ocean models, is described in section 2. By using a coupled model we avoid the very difficult task of finding the appropriate boundary conditions to drive an ocean model. The mean and standard deviation of SST and h during March and September, the peak of winter and summer in the northern oceans, are discussed in section 3. The factors which control the mean and anomalous SST tendency are examined in section 4, while the relationships between

the entrainment rate and the shear and buoyancy forcing are explored in section 5. The results are summarized and discussed in section 6.

2. Coupled model

A 50-year simulation with a global coupled atmosphere-ocean model is used to study upper ocean variability in the northern midlatitude oceans. The model consists of a Geophysical Fluid Dynamics Lab (GFDL) AGCM connected to an upper ocean mixed layer model (MLM). Alexander and Deser [1995], Battisti et al. [1995], Alexander and Penland [1996], and Bhatt et al. [1998] have used a slightly different version of the MLM to study upper ocean processes and midlatitude air-sea interaction. The ocean model consists of a grid of independent column models which include local atmosphere-ocean fluxes and the turbulent entrainment of water into the surface mixed layer, but not mean vertical motions or horizontal processes. The ocean column models are aligned with the AGCM grid over ice free regions of the global oceans. In regions with sea ice, the ice fraction, ice thickness and SST are specified.

a. atmospheric model

The GFDL AGCM is a global spectral model with rhomboidal truncation at wave number 30, which is approximately 2.25º latitude by 3.75º longitude. The model has 14 unequally spaced sigma levels in the vertical, with the lowest level at ~30 m above the surface. The model includes smoothed topography, gravity wave drag, and predicted clouds and soil moisture. Stratiform clouds form and precipitation occurs when the relative humidity exceeds 100%, while subgrid scale precipitation is parameterized by moist convective adjustment. Many features of the model's climate are presented on the World Wide Web [Collins et al., 1999], while a more complete description of an earlier version of the GCM is given by Gordon and Stern [1982] and Manabe and Hahn [1981].

b. mixed layer ocean model

The individual column models consist of a uniform mixed layer atop a layered model that represents conditions in the pycnocline. Here we use the model developed by Gaspar [1988], which has been formulated with climate simulations in mind. The temperature tendency of the mixed layer is given by:

$$\frac{\partial T_m}{\partial t} = \frac{Q_{net} + Q_{cor}}{\rho c h} - \frac{Q_{swh}}{\rho c h} + \frac{W_e \Delta T}{h} + CA - \frac{\kappa}{h}\frac{\partial T}{\partial z}\bigg|_{z=-h} \quad (1)$$

where T_m is the mixed layer temperature, $\Delta T = T_b - T_m$, T_b is the temperature of the remainder of the layer below h, Q_{net} the net surface energy flux into the ocean, Q_{cor} the surface heat flux correction, Q_{swh} the penetrating solar radiation at h, W_e the entrainment rate, ρ and c the reference density and specific heat of sea water, κ the diffusion coefficient for small scale motion, and z the vertical coordinate. Convective adjustment, *CA*, occurs when the mixed layer is more dense than the layer below, at that time heat within the remainder of the layer below h is incorporated into the mixed layer and h is then set to the top of the next layer. The model has a similar predictive equation for mixed layer salinity, where the fresh water flux is due to precipitation - evaporation (*P-E*).

The mixed layer depth primarily increases via entrainment, except in high latitudes where h can significantly deepen via *CA*. By vertically integrating the turbulent kinetic energy equation over h and then the applying a fairly standard set of assumptions [see Niiler and Krauss, 1977], W_e can be expressed as:

$$W_e = \frac{m u_*^3 - 0.5hB(h) - h\varepsilon}{h\Delta b + q^2} \quad (2)$$

where m is a constant, the surface friction velocity $u_* = \sqrt{\tau/\rho}$, where τ is the surface wind stress, and Δb is the buoyancy jump at the base of the mixed layer; following Gaspar [1988], Eq. (2) neglects mixing due to current shear across the base of the mixed layer. The buoyancy flux integrated over the mixed layer, *B(h)*, depends on Q_{net}, *P-E*, and the absorption of solar radiation in the water column. The mean turbulent kinetic energy, q^2, which is usually small but can be important for near neutral conditions, is parameterized following Kim [1976]. Mixed layer models generally differ in their parameterization of ε, the turbulent dissipation rate; here we use the formulation and parameter values given by Gaspar [1988]. When deepening by entrainment, h is computed as a prognostic variable $\left(\frac{\partial h}{\partial t} = W_e\right)$. When shoaling, the mixed layer reforms closer to the surface, W_e is set to zero, and h is computed as a diagnostic quantity by assuming a balance between wind stirring, buoyancy forcing and dissipation. When the mixed layer shoals, the temperature (salinity) profile is adjusted to conserve heat (salt) and the temperature (salinity) jump at the base of the mixed layer. The prognostic equations for T_m, S_m and h are integrated using a

first order forward in time scheme.

The region beneath the mixed layer is represented by a multi-layer system, where the temperature and salinity of the layers change by convective adjustment, vertical diffusion, and linear damping. The temperature of the upper 300 m can also change due to penetrating solar radiation. The vertical diffusion is calculated using the Crank-Nicholson scheme with a constant diffusion coefficient of 1.0×10^{-5} m s^{-2}, a value suggested by the tracer experiments of Ledwell et al. [1993]. The temperature and salinity in all model layers are damped towards their monthly mean climatological values on a 10-year time scale. This weak Newtonian damping, which crudely represents processes that vary with depth such as the mean heat transport, was necessary for the model to retain a stable density profile in regions of strong current shear. The absorption of solar radiation is parameterized following Paulson and Simpson [1977].

The bottom of the MLM is 1000 m or the actual ocean depth, which ever is smaller. For open ocean points the MLM contains 31 unequally spaced layers between the surface and 1000 m, where 15 of the layers are within the first 100 m, and the temperature and salinity of the final layer is set to the observed climatological value. The mixed layer depth is not forced to coincide with the levels of the layered model; the temperature of layers that are entirely above h are set to T_m, while T_b is from the remainder of the layer which is beneath h. However, h is constrained to be greater than 10 m and less than 850 m or the bottom of the ocean, which ever is smaller.

c. sea ice

For points where sea ice occurs during any part of the mean seasonal cycle, the MLM is not active; instead the daily ice thickness and ice fraction (or SST during ice-free periods) are specified based on the interpolated monthly mean climatology for the period 1950-95. Heat fluxes in these areas are weighted for the appropriate proportions of open water and ice. Sea ice can also form over the active MLM points, which are beyond the maximum extent of climatological ice when T_m drops to the freezing point for sea water, 271.16 K. A simple heat balance model is used for the ice, which is assumed to cover 100% of the grid box.

d. air-sea coupling and the surface heat flux correction

Heat, momentum, and fresh water are exchanged across the models air-sea interface. The net heat flux consists of the shortwave, longwave, sensible and latent heat flux. The radiative fluxes in the AGCM depend on temperature, water vapor, clouds, and specified trace constituents. The sensible and latent heat flux are computed using standard bulk aerodynamic formulas where the exchange coefficients have a constant value of 1.0×10^{-3}. The surface wind stress is computed in a similar fashion. The wind speed, air temperature and specific humidity used in the bulk formulas are taken directly from the lowest model level, while the SST is given by T_m obtained from the ocean model. The atmosphere and ocean models exchange information once per day, the time step of the MLM. The atmosphere-to-ocean fluxes are averaged over the 96 time steps in one AGCM day, while the ocean-to-atmosphere fluxes are computed every AGCM time step using the daily SST values.

Due to errors in the surface fluxes and processes absent from the ocean model it is necessary to correct the surface fluxes in order for the simulated climate to remain close to observations [Sausen et. al., 1998; Manabe and Stouffer, 1988; Battisti et al., 1995]. Here the surface heat and salt flux corrections are obtained from a 20-year MLM simulation using surface fluxes from a separate GFDL AGCM run, where the AGCM had observed climatological SSTs as boundary conditions. Prior to each time step, the SST is set to the observed climatological value on that day. The observed daily SSTs were obtained by interpolating the monthly values of Smith et al. [1996] onto the R30 grid. The MLM is then run for one time step where T_m and h are free to evolve. The difference between the predicted T_m and observed SST is used to compute the heat flux correction necessary for the model to match observations. A similar method is used to obtain the salt flux correction. This procedure is repeated to obtain 20 years of daily flux correction values. Long term monthly mean corrections are computed and then linearly interpolated to daily values which are then added to the temperature and salinity tendency equations but not the entrainment equation.

The flux corrections vary with location and time of year but do not vary from one year to the next. The annual mean surface heat flux correction, Q_{cor}, is shown in Fig. 1 for the North Atlantic and Pacific Oceans. Heat is added to the oceans in the western ~1/2 of both basins, with maxima of ~150 W m^{-2} to the east of Japan and the east coast of the United States. The magnitude and pattern of $-Q_{cor}$ resembles the observed annual mean Q_{net} and equivalently the mean oceanic heat flux convergence [Hsuing, 1985; Moisan and Niiler, 1998], indicating that the correction is primarily accounting for the absence of advection in the ocean model. Q_{cor}

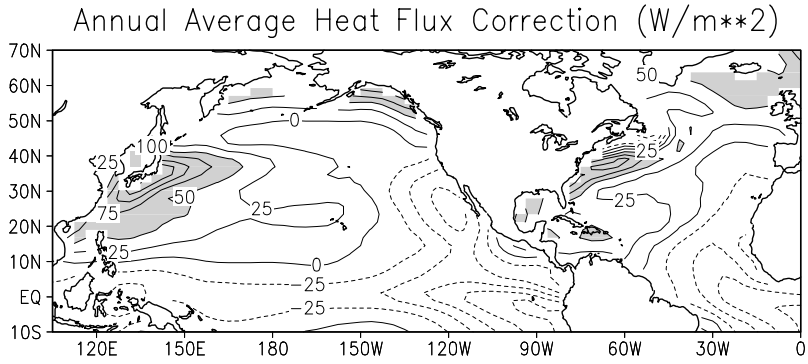

Fig. 1. Annual average surface heat flux correction (Wm^{-2}). Positive values indicate heat is added to the ocean. The contour interval is 25 and values greater than 50 are shaded. This figure and all subsequent planar plots have been smoothed using a 9-point filter.

exceeds 300 W m^{-2} in the vicinity of the Kuroshio Current and Gulf Stream in March, but is negligible in September (not shown), due to the large seasonal cycle in heat transported by these current systems [Wilkin et al., 1995; Yu and Malanotte-Rizzoli, 1998]. The GFDL AGCM, like many current climate models, overestimates the shortwave radiation reaching the surface, primarily due to errors in simulating clouds [Garratt et al., 1998]. As a result, Q_{cor} values between -50 and -100 Wm^{-2} are applied to the MLM during summer from 40ºN-60ºN.

e. initial conditions

The initial ocean conditions for the coupled model integration were derived by averaging the MLM variables on January 1st for 20 years of an MLM simulation driven by surface fluxes from a previous AGCM simulation. The atmospheric conditions were obtained for January 1st by integrating the GFDL AGCM for five years beginning from a state of rest. Since the AGCM and MLM initial conditions were obtained independently, there is an adjustment period of a few months once the two models are coupled.

3. SST and *h*

Here we examine sea surface temperature and mixed layer depth fields from the 50-year coupled atmosphere-ocean integration and compare them to observations. The simulated and observed long-term monthly mean SST differ by less than 1ºC at nearly all of the MLM grid points (not shown), a result of imposing a surface flux correction. However, these small differences are systematic: the simulated SSTs tend to be too warm (cold) in summer (winter). These model biases are due to nonlinearities in the MLM, computing the flux corrections from a 20-year ocean only integration, and the method used to interpolate the flux corrections in time did not preserve the monthly means from which they were computed.

The observed and simulated interannual standard deviations (σ) of SST in March over the Northern Hemisphere Oceans are shown in Fig. 2. The standard deviations are computed from the departures of the individual monthly means from the long term monthly means. The observed σ values are derived from the Smith et al. [1996] data set for the period 1950-95, while the simulated values are from the 50-year model integration. Both the simulated and observed σ range from 0.3º to 1.2ºC over the open ocean. In the Atlantic, σ is maximized along the east coast of North America, in part due to the variability in wind speed and air temperature associated with continental air masses moving over the ocean. However, only the observations exhibit a band of enhanced σ that extends from the mid-Atlantic states to east of Newfoundland, which likely arise due to variability in Ekman transport across strong SST gradients [Luksch, 1996] and in heat transport by the Gulf Stream and North Atlantic Current. The March σ exceeds 0.6ºC in the central North Pacific in both the model and observations, but the maximum variability of ~0.8ºC occurs 10º-15º farther south in the model. The simulated SST variability is also greater (less) than observed in the South China Sea (Gulf of Alaska). Since the coupled model does not contain horizontal processes such as currents and wave dynamics, there is no El Niño/ Southern Oscillation (ENSO), and σ is significantly underestimated in the eastern tropical Pacific (Fig. 2).

Fluctuations in the strength and position of the Aleutian low associated with ENSO have been shown to cause SST anomalies to form in the North Pacific primarily through changes in Q_{net} [Alexander, 1992; Luksch

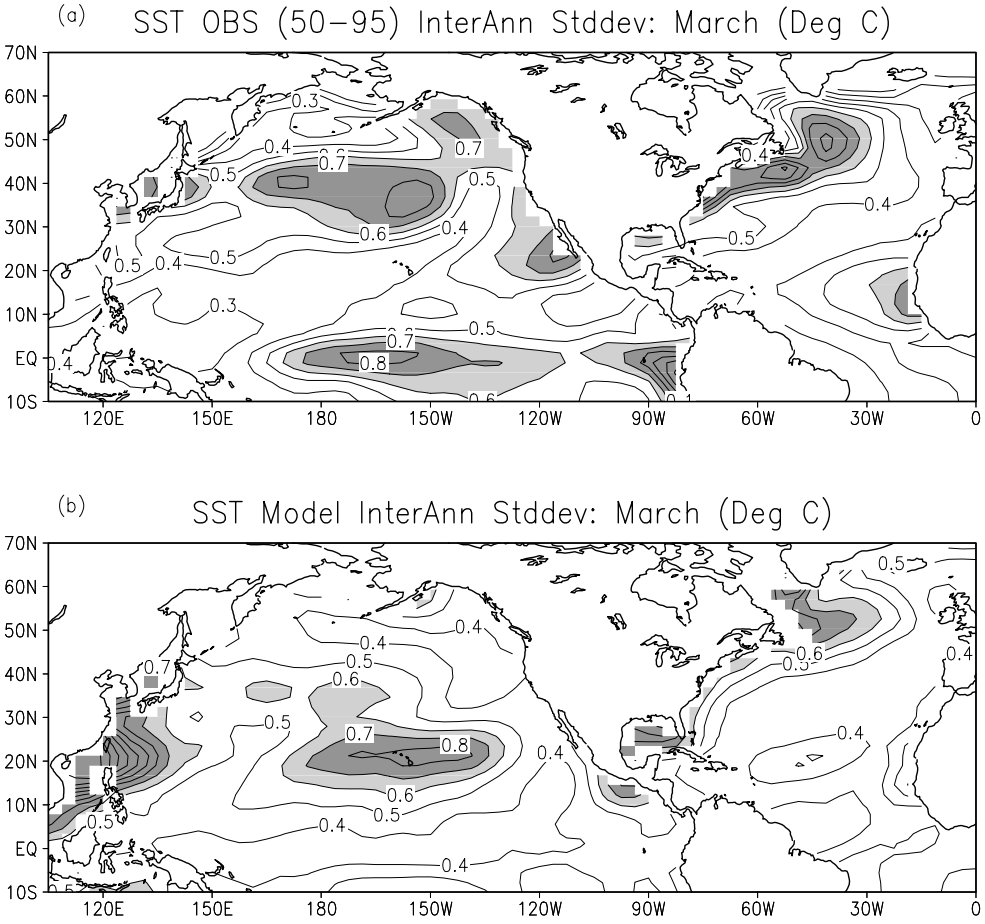

Fig. 2. The standard deviation ( )of March SSTs (˚C) from (a) observations and (b) the 50-year coupled model simulation. The observed SSTs, which extend from 1950-95, are originally from the data set of Smith et al. (1996) which have then been interpolated from a 2˚x2˚ grid to the R30 Gaussian grid. The contour interval is 0.1˚C, and 0.6˚C<SST <0.8˚C is shaded light while those greater than 0.7˚C are shaded dark.

and von Storch, 1992; and Lau and Nath, 1996). We have examined the influence of ENSO on midlatitude SSTs using an additional GFDL AGCM-MLM experiment where observed SSTs are specified between approximately 25˚N-25˚S in the Pacific for the period 1950-1995 and SSTs are provided by the MLM elsewhere over the global oceans. Including the observed ENSO signal generally improves the simulation of SST variability in the North Pacific, including: a ~15º northward shift in the maximum SST σ to 30ºN-40ºN in the central Pacific; a decrease in σ in the Sea of Japan; and a slight increase in σ in the northeast portion of the basin (not shown).

The SST σ from observations and the model simulation during September are shown in Fig. 3. Both the observed and simulated variability are greater in September than in March, primarily due to the relatively small thermal inertia of the shallow mixed layer in summer (see section 4). The observed SST σ in September exceeds 0.6ºC over both oceans between 30ºN-50ºN and reaches a maximum of 1ºC along 40ºN in the Pacific. The simulated σ also exceeds 0.6ºC in both basins but the region of enhanced variability is located about 15º farther south in the Atlantic compared to observations. While the region of SST σ > 0.6ºC is close to that observed in the North Pacific, it extends too far south in the central Pacific and does not cover the eastern Pacific from 20ºN-35ºN. The model simulates regions where σ > 0.7ºC in the North Pacific but it is too broad compared to observations.

Studies by Norris and Leovy [1994] and Norris et al. [1998] indicate that variability in stratus clouds contributes to SST anomalies in the central North Pacific during summer. As discussed in section 2, the GFDL model like most AGCMs have difficulty simulating clouds, especially low-level stratus decks. Thus, some of the differences between the observed and simulated SST σ in September may result from errors in the in simu-

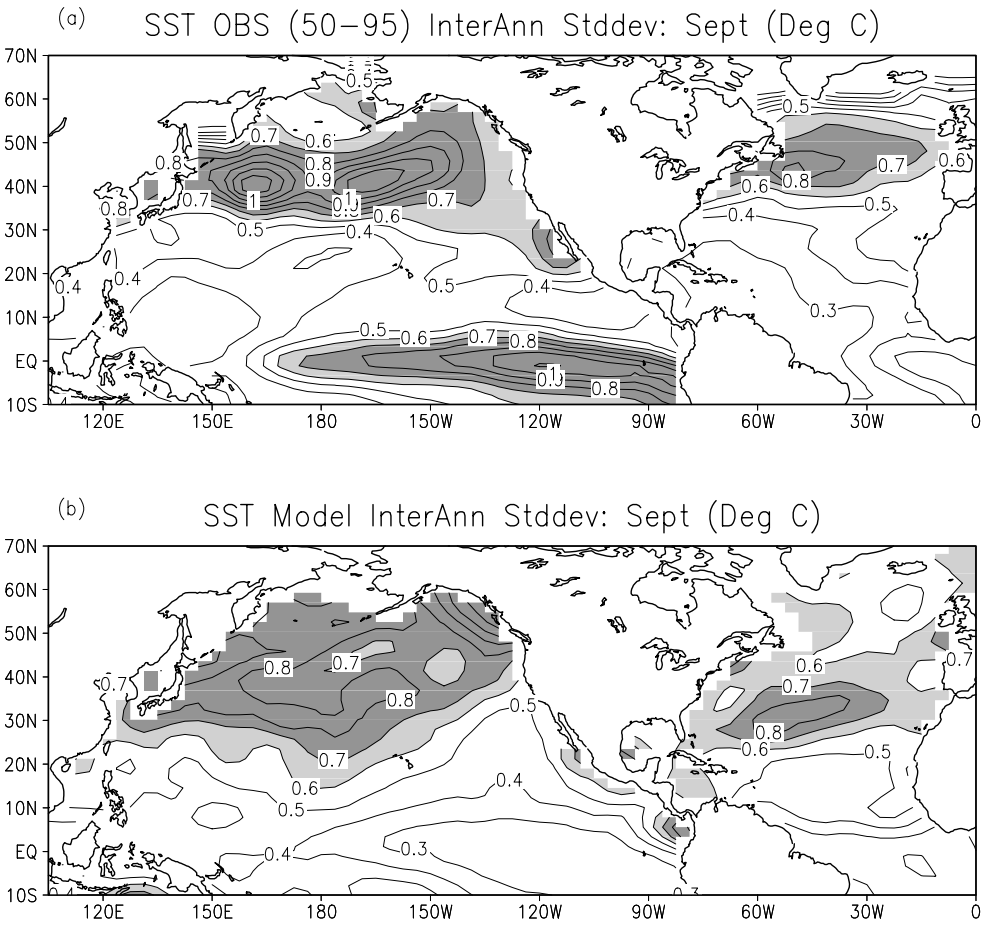

Fig. 3. The (a) observed and (b) simulated standard deviation of September SSTs (˚C). Contour interval and shading as in Fig. 2.

lated stratus clouds and the attendant surface shortwave radiation.

As expected, the model strongly underestimates the SST variability associated with ENSO in the tropical Pacific during September. Unlike March, there is no clear change in the pattern or strength of the variability outside of the tropical Pacific in the model simulation which included the specified ENSO signal. This is consistent with Horel and Wallace [1981], Mitchell and Wallace [1996] and Kumar and Hoerling [1998] who found that the extratropical atmospheric changes associated with ENSO are much greater in winter than summer.

The observed and simulated mean mixed layer depth, *h*, are shown in Fig. 4 for March. The observed *h* is obtained from Monterey and Levitus [1997] based on the depth where the density is 0.0125 kg m^{-3} less than the surface density. The observed *h* values, which were originally on a 1ºx1º grid, have been interpolated onto to the models Gaussian grid.

The observed mixed layer reaches its greatest depth in the North Atlantic where it exceeds 500 m from the Labrador Sea to east of Scotland. In nature, the formation of deep water through complex convective processes can lead to instantaneous mixed layer values of greater than 1500 m in the Labrador and Greenland Seas [Gascard and Clarke, 1983; Dickson et al., 1996]. A secondary maximum in the observed *h* extends northeastward across the central Atlantic. The MLM simulates the observed structure of *h* but underestimates its magnitude especially north of ~45ºN.

The observed March mixed layer depths are much smaller in the Pacific where there is no deep water formation. The observed *h* reaches a maximum value of ~200 m, slightly greater than *h* in the coupled model integration. The observed and simulated *h* maxima are located in the western Pacific between 30ºN-45ºN, but the center of this maximum is located 5º to the south and closer to the coast in the model. The elongated regions of enhanced *h* between 30ºN-50ºN in both oceans are coincident with the surface forcing associated with the main storm tracks [Alexander and Scott, 1997]. Unlike

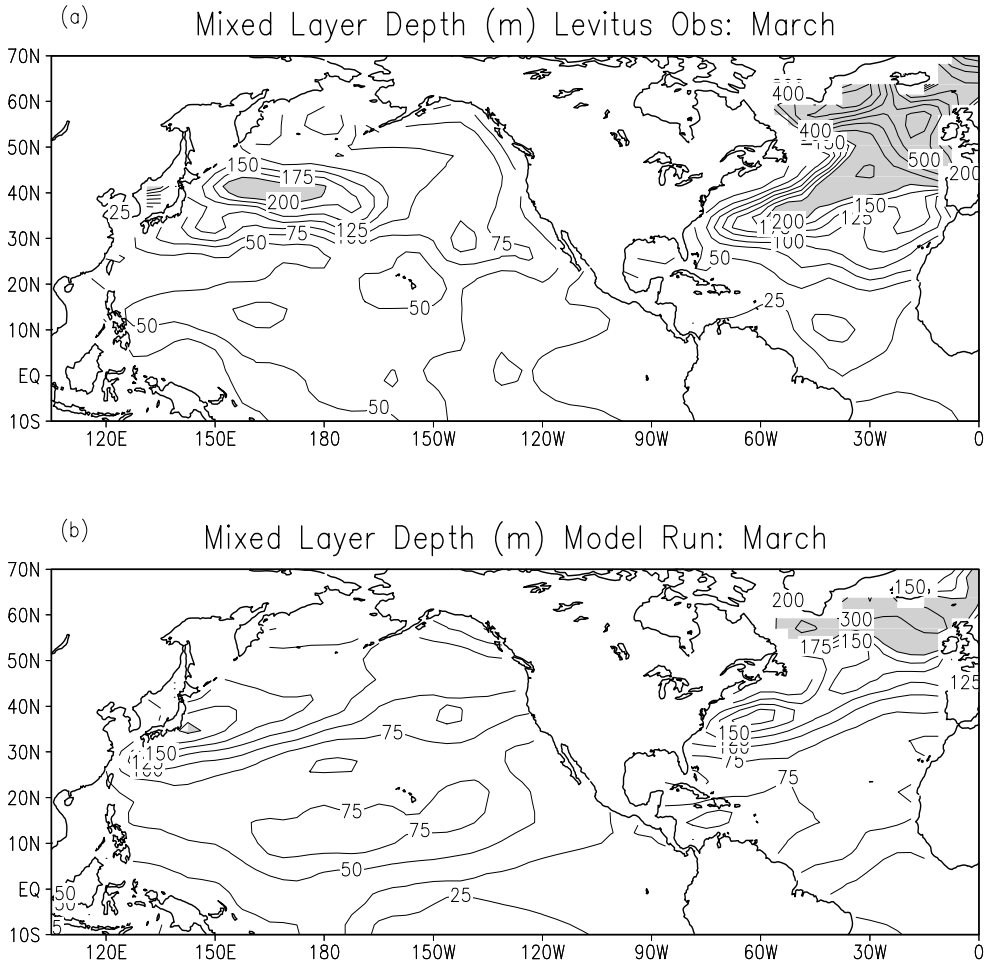

Fig. 4. The (a) observed and (b) simulated mixed layer depth (m) in March. The observed *h* values are from Monterey and Levitus (1997) which have then been interpolated from a 1˚x1˚ grid to the R30 grid.. Note that the contour interval changes: it is 25 for $h < 200$ and 100 for $h > 200$; values greater than 200 are shaded.

observations, the model does not contain a narrow region of shallow *h* along the west coast of North America perhaps due to the absence of coastal upwelling in the MLM. The observed and simulated *h* range between 25-75 m throughout the tropics.

Several factors may contribute to the underestimation of *h* during winter in the coupled model simulation: (i) The MLM tends to shoal too rapidly under stable conditions and thus may be unable to maintain deep mixed layers through late winter. (ii) Many ocean processes which generate turbulence are not included in the MLM, such as surface wave breaking, Langmuir cells, inertial current shears, etc. (iii) The surface mechanical forcing is proportional to the cube of the wind speed and the buoyancy forcing depends on the square of the wind speed; thus *h* deepens significantly during short periods of high wind speed. The surface boundary conditions are averaged over one day, which suppresses extreme short-duration forcing. (iv) The mixed layer is constrained to be less than 850 m in the MLM, thereby limiting *h* when deep convection occurs. (v) The MLM does not include currents, which limits *h* due to the absence of mixing due to vertical shear and the advection of heat and salt which can change the vertical stability of the water column. Both of these processes are likely to be important in the western boundary currents and the subpolar gyre of the North Atlantic, where the MLM greatly underestimates *h*. (vi) The observed mixed layer depth is estimated from the mean temperature and salinity profiles, while in the MLM *h* is the layer over which surface generated turbulence is active.

The observed and simulated mixed layer depths are at a minimum in June-August (not shown) but are still quite shallow in September (Fig. 5). The model closely approximates observations with *h* on the order of 20 m in the central North Atlantic and much of the

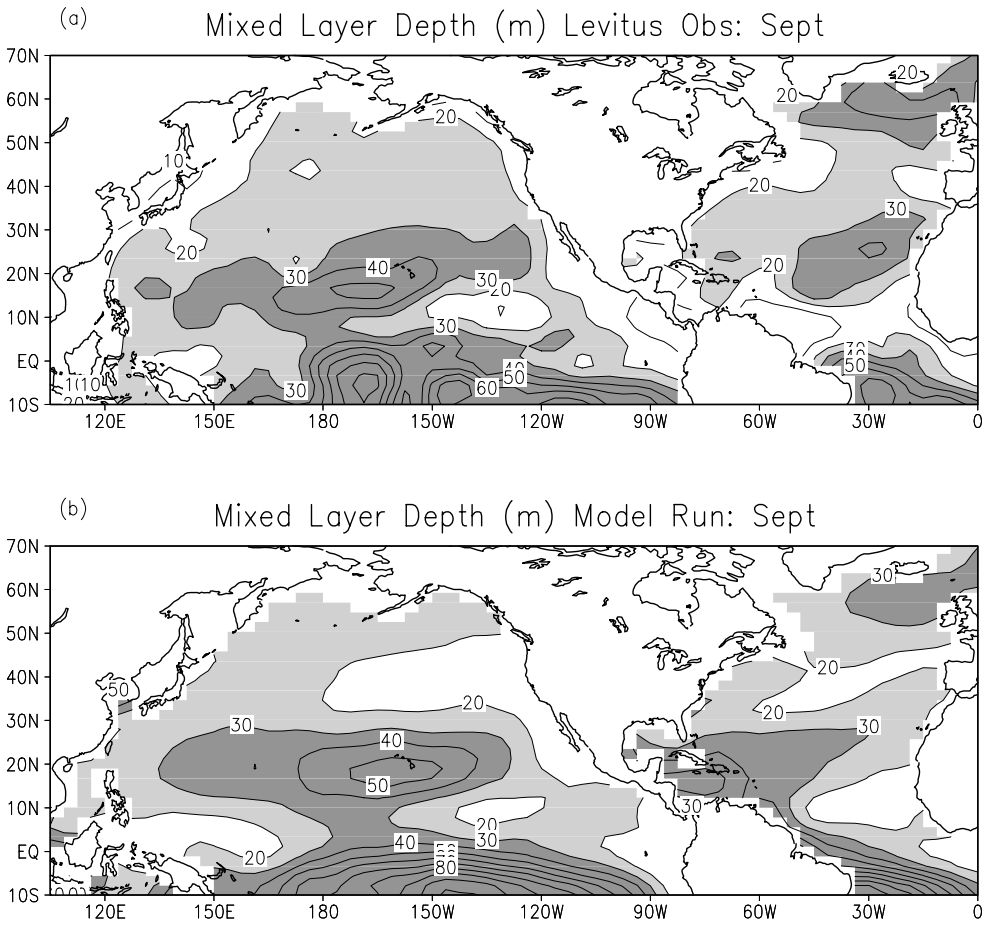

Fig. 5. The (a) observed and (b) simulated mixed layer depth (m) in September. The contour interval is 10, where 20< h<30 is shaded light and h> 30 is shaded dark

North Pacific, and somewhat deeper mixed layers north of 50ºN in the Atlantic and in the subtropics of both ocean basins. The MLM also reproduces the observed minimum in h between 0º-10ºN and the deepening of the mixed layer from 0º to10ºS.

Basin-wide estimates of the interannual standard deviation of mixed layer depth are not available from observations; the simulated σ of h are shown in Fig. 6 for March and September. The regions of greatest variability coincide with the maximum mean h values both in winter and summer (c.f. Figs. 4 and 5). The σ of h is greatest in the north Atlantic in March where it exceeds 30 m north of ~30ºN and 60 m from about 45ºN-65ºN. While h σ in March exceeds 30 m over much of the northwest Pacific and in the vicinity of Hawaii, it is less than 60 m over the entire Pacific. The variability is greatly reduced in September when the σ of h < 5 m over much of the ocean between 30ºN-60ºN and has a maximum of 15-20 m at 15ºN and 10ºS in the central Pacific and western Atlantic.

4. Components of the SST tendency equation

The factors which control the SST tendency in the MLM, shown on the right hand side of Eq. 1, are associated with fluxes through the surface and the base of the mixed layer. Multiplying Eq. 1 by ρch gives the terms in flux form: the net surface heat flux (Q_{net}); surface flux correction (Q_{cor}); penetrating solar radiation (Q_{swh}), entrainment heat flux (Q_{we} = ρ$cW_e\Delta T$); convective adjustment (CA); and temperature diffusion at h (T_{dif}). The seasonal cycle of the zonal average of these 6 terms, obtained from the long term monthly means of the simulated fluxes, are shown in Fig. 7.

As expected, Q_{net} is the dominant term over much of the Northern Hemisphere, with magnitudes exceeding 80 Wm^{-2} north of 20ºN in summer and winter. Heating due to solar radiation in summer and cooling by the sensible and latent heat fluxes in winter results in a strong seasonal cycle of Q_{net} with a maximum ampli-

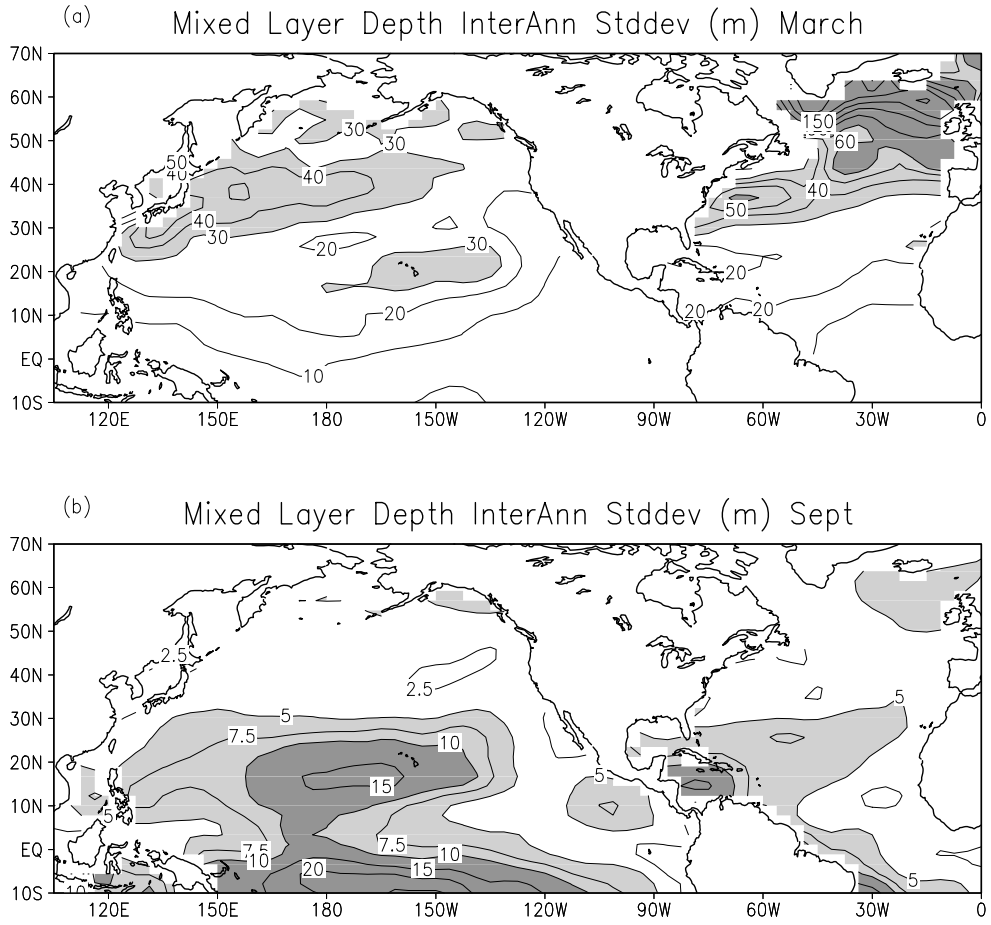

Fig 6. The simulated standard deviation of mixed layer depth (m) in (a) March and (b) September. In (a) values of $h\sigma$<30 m have a contour interval of 10 and are shaded light, while $h\sigma$ > 30 m have a contour interval of 30 and are shaded dark. The contour interval in (b) is 2.5 where 5< $h\sigma$<10 is shaded light and $h\sigma$ >10 is shaded dark.

tude of 200 Wm^{-2} at ~40ºN. However, the total flux through the surface is reduced by Q_{cor} which is roughly half as large as Q_{net} but of opposite sign. Q_{we} acts to cool SSTs over most of the Northern Hemisphere, since W_e is always positive and ΔT ($=T_b-T_m$) is negative over most of the worlds oceans. When $|\Delta T|$ reaches a maximum in fall, Q_{we} is similar in magnitude to Q_{net}, exceeding |80| Wm^{-2} between 35ºN-60ºN. The other three components, *CA*, Q_{swh} and T_{dif}, are substantially smaller (note that the contour interval is 1/4 as large compared with the other 3 components) over most of the globe. *CA* is negligible except at high latitudes in winter when episodic deep convection brings warm salty water into the mixed layer. Q_{swh} cools the mixed layer, primarily in the subtropics in summer when the surface solar radiation is a maximum and h is a minimum. Like entrainment, T_{dif} acts to cool the mixed layer primarily at mid latitudes in fall when $|\Delta T|$ is a maximum.

The σ values for Q_{net} and Q_{we}+*CA* over the course of the seasonal cycle, shown in Fig. 8, are computed from the departure of monthly means from the 50-year mean at each model grid point which are then zonally averaged. Recall that the seasonal cycle of the flux correction is the same each year (Q_{cor} σ = 0). W_e have combined *CA* with Q_{we} since the former represents convective plumes, an extreme form of entrainment. The Q_{net} σ has a maximum in winter opposite to the mean Q_{net}. However, the simulated variability of Q_{net} may be underestimated due to the lack of low cloud variability. The seasonal cycle of the σ of Q_{net} tends to lag the mean by about one month, e.g. the magnitude of the mean (σ) Q_{net} is maximized in January (February). The Q_{we}+*CA* σ has two maxima exceeding 25 Wm^{-2}, one at high latitudes in winter and the second in midlatitudes in fall; the former (latter) is due to variability in *CA* (Q_{we}). The general zonal structure of the σ of Q_{swh} and T_{dif} resem-

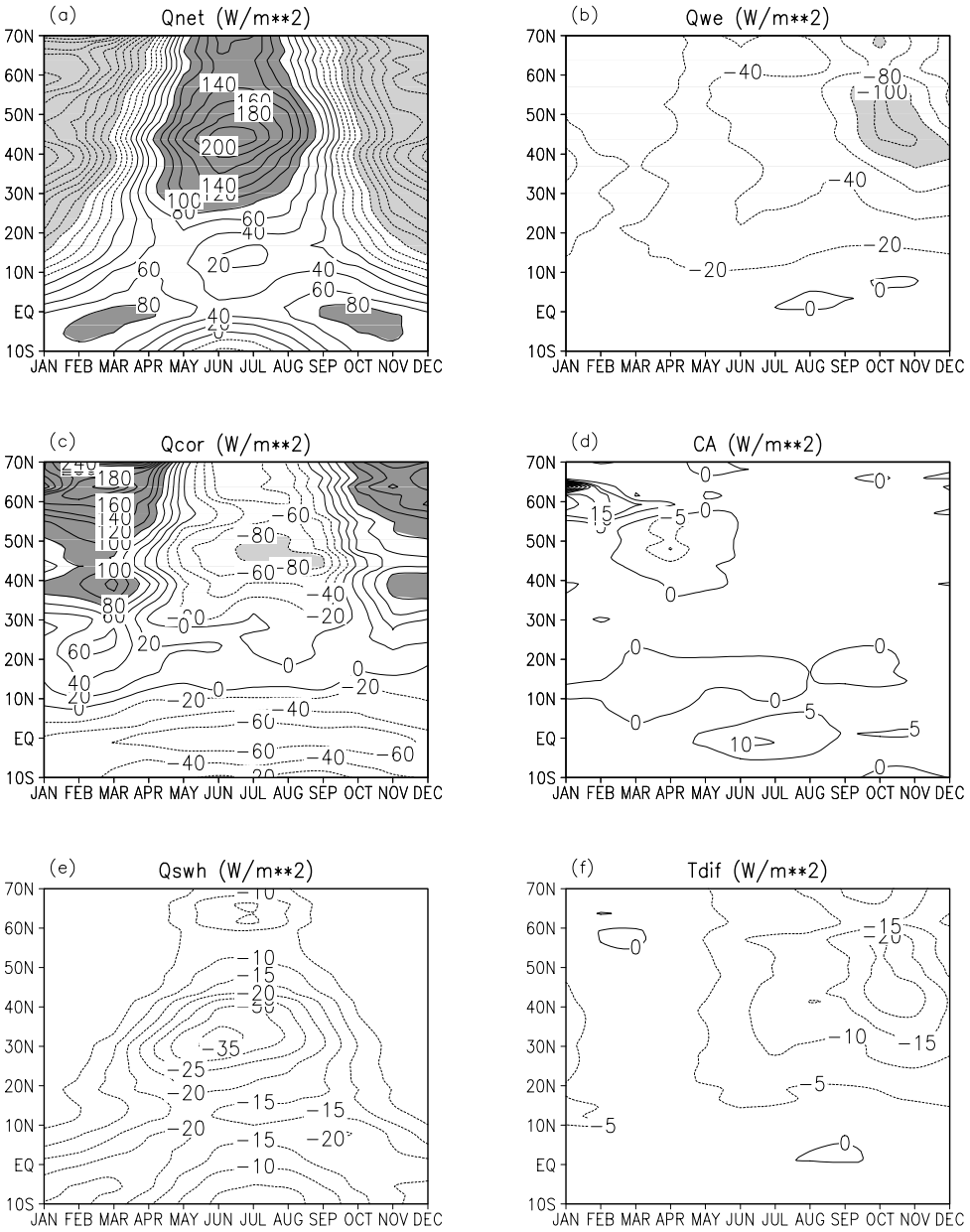

Fig. 7. Zoally averaged (a) net surface heat flux, (b) entrainment heat flux, (c) surface heat flux correction, (d) convective adjustment (e) penetrating solar radiation, and (f) temperature diffusion (Wm^{-2}) in the MLM as a function of calendar month. The contour interval is 20 in (a)-(c) and 5 in (d)-(f). Negative contours are dashed and values <-80 (>80) are shaded light (dark).

ble their means, with maximum values of 8 and 4 Wm^{-2}, respectively (not shown).

The spatial structure of Q_{net} in the R30 version of the GFDL is in general agreement with observations [Alexander and Scott, 1997]. The mean Q_{we}+*CA* from the coupled model simulation in March and September are shown in Fig. 9. During March Q_{we}+*CA* is relatively weak over both ocean basins with the strongest cooling (< -30 Wm^{-2}), south of Japan, at 10˚N in the central Pacific, and at 50˚N in the central Atlantic. *CA* leads to warming (> 30 Wm^{-2}) south of Greenland (not shown). In September, when *CA* is negligible, Q_{we} is fairly zonal in structure and decreases poleward. The maximum cooling occurs in the northwestern Pacific, where the magnitude of Q_{we} exceeds 100 W m^{-2}, roughly twice that in the Atlantic at the same latitude. Q_{we}+*CA* weakly warms the tropical Pacific as $\Delta T > 0$. In this region, P-E > 0 increases the surface buoyancy creating a shallow

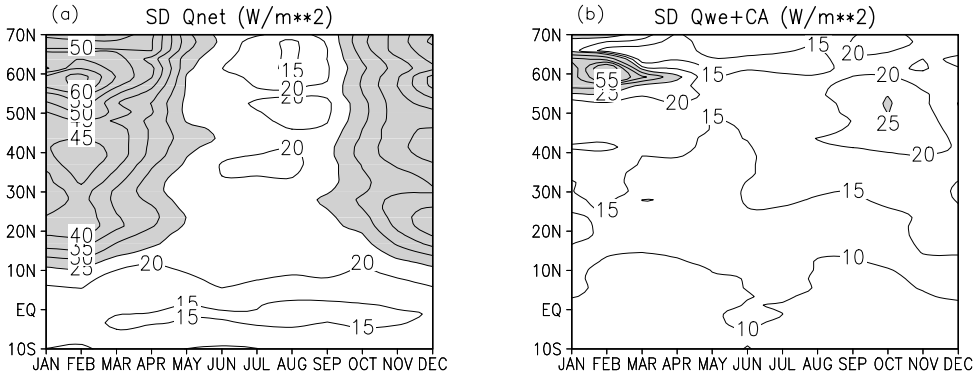

Fig. 8. Zonally averaged standard deviations of (a) the net surface heat flux and (b) the heat flux due to entrainment plus convective adjustment (Wm^{-2}) as a function of calendar month. Q_{net} and $Q_{we} + CA\,\sigma$ are computed using monthly anomalies at each MLM grid point and then zonally averaged. The contour interval is 5, values greater than 25 are shaded.

mixed layer (Figs. 4 & 5) that is often maintained by a jump in salinity. Observational studies by Lukas and Lindstrom [1991] and Anderson et al. [1996] also indicate that entrainment acts to slightly warm the mixed layer and helps to maintain high SSTs in the tropical West Pacific. The warming due to Q_{we}+CA in the eastern equatorial Pacific during September in the model is unrealistic.

Previous studies [e.g. Cayan, 1992; Iwasaka and Wallace, 1995; Delworth, 1996; Deser and Timlin, 1997] along with Fig. 8 indicate that variability in Q_{net} plays an important role in the development of SST anomalies. Here, we assess the relative importance of entrainment in generating SST variability by taking the ratio of (Q_{we}+CA)σ to $Q_{net}\sigma$ during March and September (Fig. 10). During March (Q_{we}+CA)σ/$Q_{net}\sigma$ is small, between 0.2-0.4, over most of the ocean north of 10˚S, except for the tropical West Pacific and in the Atlantic north of 30˚N. Ratios which exceed unity in the North Atlantic are due to CA rather than Q_{we}. The (Q_{we}+CA)σ also exceeds that of $Q_{net}\sigma$ in the vicinity of the equator near 160˚E, which may be related to interannual variability in the strength of the Madden-Julian Oscillation [Shinoda and Hendon, 1998].

Variability in the entrainment heat flux clearly plays an important role in generating SST anomalies during September over much of the Atlantic (Pacific) north of 45˚N (35˚N) where (Q_{we}+CA)σ/$Q_{net}\sigma$ > 1.0. During summer most of the heat flux across the base of the mixed layer is associated with mixing in a convectively stable environment , and thus $Q_{we}\,\sigma >> CA\,\sigma$.

The development of the simulated SST anomalies, due to surface heat fluxes and entrainment, the dominant processes in the MLM, is examined further by decomposing the variables in Eq. 1 into daily mean ($\overline{\ }$) and departures (‘) from the mean. Clark [1972] and Alexander and Penland [1996] have performed a similar analysis, using the approximation $1/(\overline{h+h'}) \approx 1-(h'/\bar{h})$, which is valid only when $h'/\bar{h} < 1$, a condition that is violated over parts of the ocean especially in spring and summer. Here, $h \equiv 1/\eta$, then using Eq. 1 the anomalous T_m tendency can be written as :

$$\frac{\partial T'_m}{\partial t} = \underbrace{\frac{Q'_{net}\bar{\eta}}{\rho c}}_{I} + \underbrace{\frac{(\overline{Q_{net}}+\overline{Q_{cor}})\eta'}{\rho c}}_{II} + \underbrace{\frac{Q'_{net}\eta' - \overline{Q'_{net}\eta'}}{\rho c}}_{III}$$

$$+ \underbrace{W'_e\overline{\Delta T\eta}}_{IV} + \underbrace{\overline{W_e}\Delta T'\bar{\eta}}_{V} + \underbrace{\overline{W_e\Delta T}\eta'}_{VI}$$

$$+ (W'_e\Delta T' - \overline{W'_e\Delta T'})\bar{\eta} + (W'_e\eta' - \overline{W'_e\eta'})\overline{\Delta T}$$

$$+ (\Delta T'\eta' - \overline{\Delta T'\eta'})\overline{W_e} + W'_e\Delta T'\eta' - \overline{W'_e\Delta T'\eta'} + CA' \quad (3)$$

Composites of the individual terms in (3) are constructed at each model grid point based on when the local monthly value of $\frac{\partial}{\partial t}T'_m > 1\sigma$ Composites are computed for each calendar month by summing daily values of each term during the months when the σ criteria is exceeded. Approximately 10 months of data went into each composite.

Analyses of zonal means of the terms in Eq. 3 indicates that only the first six make a significant contribution to T_m anomaly development and that the contribution of the individual terms is distinctly differ-

ent in the tropics and midlatitudes but relatively uniform north of ~20ºN (not shown). Fig. 11 shows the seasonal cycle of the first six terms on the right hand side of (3) averaged between 20ºN-70ºN. Term I is dominant through out the year, indicating that Q'_{net} strongly contributes to the fastest growing SST anomalies. Even though Q'_{net} is 2-3 times larger in winter than summer (Fig. 8), $\eta\ (=1/\bar{h})$ is an order of magnitude smaller in winter than summer (Figs. 4&5), as a result term I ranges from about 0.4ºC mon^{-1} in January to 1.0ºC mon^{-1} in July. Term II plays an important role in generating SST during spring and summer, in general agreement with Clark [1972] and Alexander and Penland [1996], although they estimated its impact to equal or exceed Term I. Term III depends on how the instantaneous relationship between Q_{net} and η differs from their long term correlation. The net surface heating causes a more buoyant and thus shallower mixed layer, which results in a positive correlation between Q'_{net} and η'. During early spring the distribution of η' is highly skewed, since the mixed layer tends to shoal abruptly but only gets marginally deeper than the mean. As a result, $\overline{Q'_{net}\eta'} > \overline{Q'_{net}}\,\overline{\eta'}$ and thus term III makes a significant contribution in February-April to the positive $\frac{\partial}{\partial t}T'_m$ composite, but is negligible for the negative composite (not shown). Term IV, associated with the anomalous entrainment rate, is maximized in July when it contributes ~ 0.4˚C mon-1 to SST anomaly growth. Positive values of term IV result from weaker entrainment of colder water from below (W'_e<0), since $\overline{\Delta T} = \overline{T_b - T_m} < 0$ and $\bar{\eta} > 0$. Term V, which represents the mean entrainment of the anomalous temperature jump at the base of the mixed layer, reaches a maximum in September, when $\Delta T'$ and $\bar{\eta}$ are large. Term VI always acts to damp SST anomaly growth, as $\overline{W_e}$ is positive, $\overline{\Delta T}$ is almost always negative, and the mixed layer

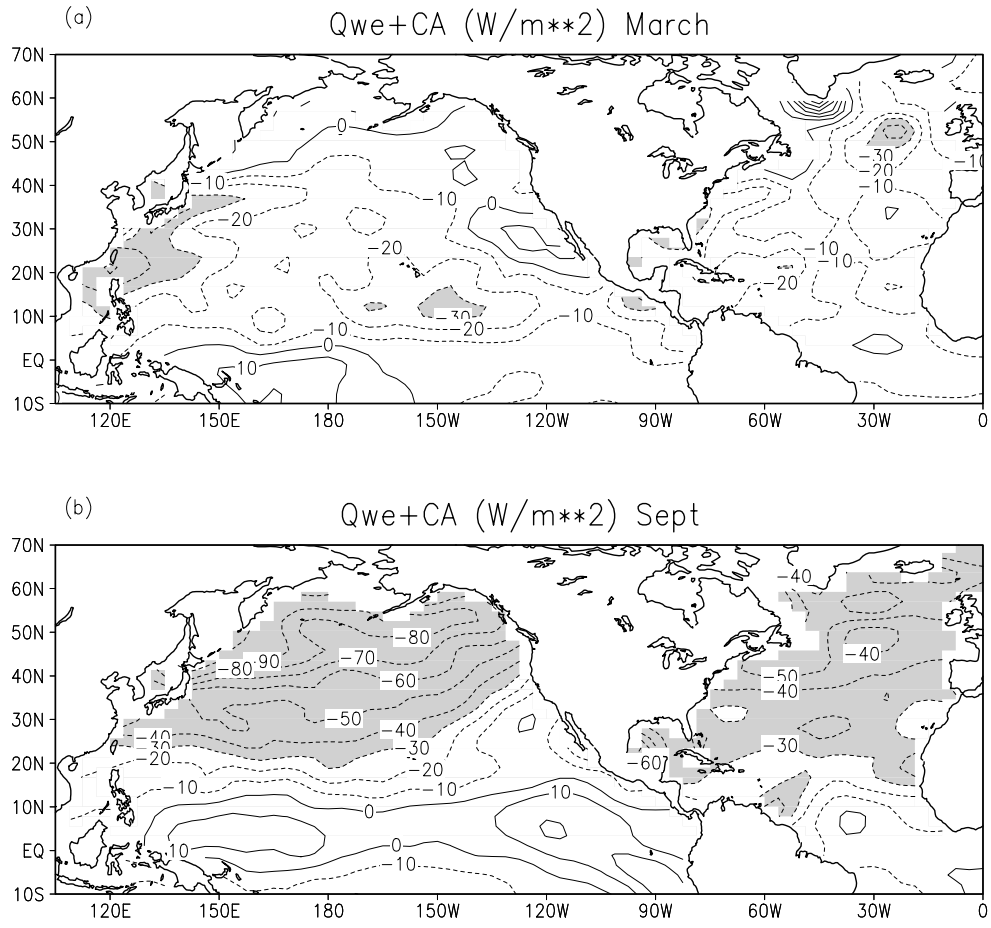

Fig. 9. The heat flux due to entrainment plus convective adjustment (Wm^{-2}) in (a) March and (b) September. The contour interval is 10, values less than 30 are shaded.

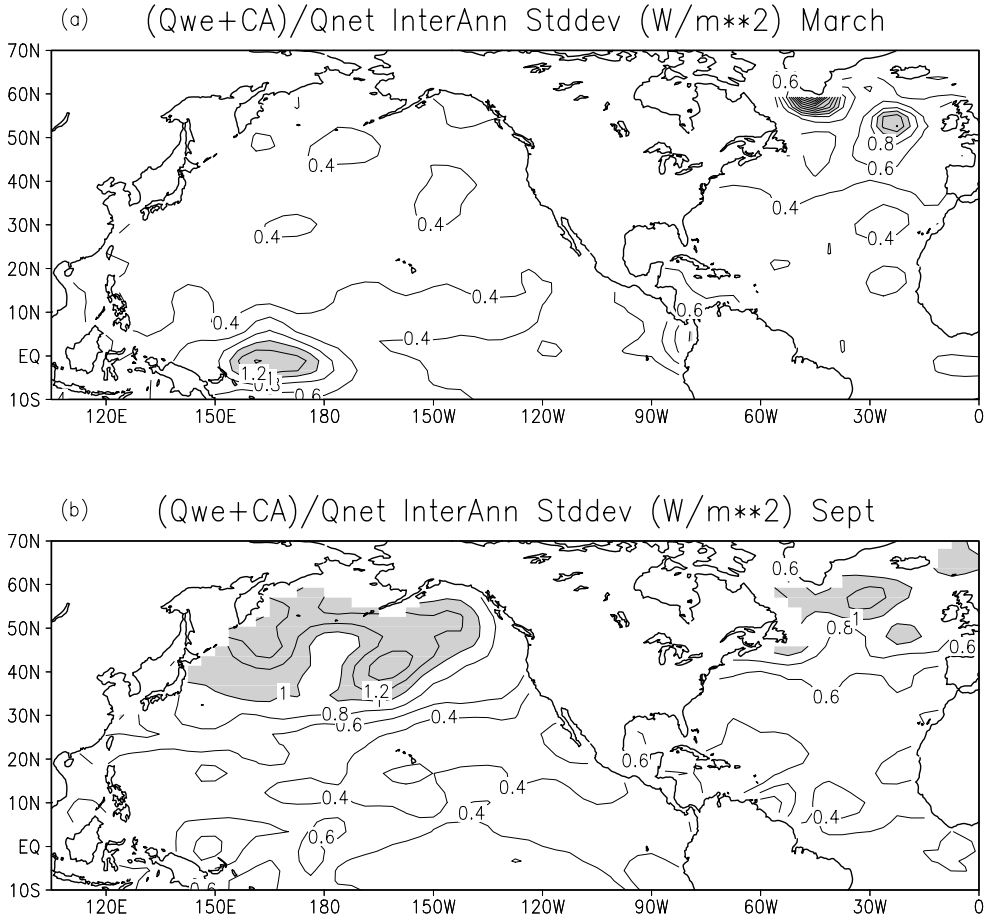

Fig 10. The standard deviation of entrainment heat flux plus convective adjustment divided by the standard deviation of the net surface heat flux $(Q_{we}+CA)\sigma/Q_{net}\sigma$ in (a) March and (b) September. The contour interval is 0.2, values greater than 1.0 are shaded.

tends to be shallower (η'>0) when it is warming rapidly.

5. Components of the entrainment equation

The entrainment rate in the MLM, given by Eq. 2, is governed by u_*^3, *B(h)* and Δb which represent wind stirring, buoyancy forcing integrated over the mixed layer, and the buoyancy jump at the base of the mixed layer, respectively. Correlations between these three terms and W_e, are computed for each calendar month using daily anomalies of u_*^3, *-B(h)* and -Δb only on days when entrainment has occurred. Negative values of *B(h)* and Δb anomalies should enhance entrainment all other factors being equal. Averages of the correlations for all of the ocean model grid points between 20ºN and 70ºN are shown in Fig. 12. The correlation between W_e and u_*^3 anomalies ranges between about 0.35 in February to 0.6 in June. In contrast, the correlations between W_e and *-B(h)* peak near ~0.6 in winter and decrease to ~0.3 in summer. Correlations between W_e and -Δb, while generally small, approach ~0.3 in fall.

The analysis above examines the linear relationship between W_e and the anomalous forcing terms. In some mixed layer models, including the one described by Niiler and Krauss [1977], dissipation is a constant fraction of the individual forcing terms, so their contribution to W_e can be determined independently [Hanson, 1992]. In the MLM dissipation is non-linear: ε in Eq. 2 is a complex function of B(h), u_*^3 and u_*/f, where f is the coriolis parameter. However, a non-dimensional mixing efficiency can be defined:

$$P^* = h\Delta b W_e / u^{*3} \qquad (4)$$

which is solely a function of *h*/L and *h*/λ [Gaspar, 1988], where $L(=u_*^3/B(h))$ is a bulk Monin-Obukov length

scale and $\lambda(=u_*/f)$ is the Ekman or Rossby rotation scale. Contoured values of $P^*(h/L, h/\lambda)$ are shown in Fig. 13. P^* increases as h/L decreases since more surface cooling ($B(h) < 0$) leads to enhanced mixing. P^* decreases as h/λ increases since rotation limits the vertical size of eddies. However, h/λ has a negligible impact on P^* for values of $h/L < \sim 5$.

A scatter plot of 50 years of monthly mean values of h/L verses h/λ averaged between 20˚N-70˚N obtained from the coupled model simulation are also shown in Fig. 13. From September through April the seasonal cycle dominates the interannual variability, as all 50 values within a given month reside in a distinct area of the h/L, h/λ phase space. The spread in the individual monthly values of h/L and thus P^* is largest in January and February. The maximum values of h/L (h/λ) occur in December-February (January-March), while the minimum of both length scales occurs in June-July. Fig. 13 suggests that entrainment occurs much more often than shoaling, since P^* is almost always greater than zero. While P^* appears to depend much more strongly on L than λ, at a given time and location variations in λ can influence entrainment, especially from March through September.

The mean seasonal cycle of h/L versus h/λ in Fig. 13 displays a "hysteresis loop": with a different path through the h/L, h/λ phase space in the first and second half of the year. The hysteresis loop results from lags in the seasonal cycle between $B(h)$, u_*, and h; zonal averages of the quantities reach a maximum in November, January, and March, respectively. Hysteresis loops in the seasonal cycles of heat content and SST or potential energy have been discussed by Gill and Turner [1976]. Fig. 13 along with previous studies indicate that the hysteresis effect in the upper ocean depends on lags between the surface heating and mechanical forcing and on the physics of the mixed layer, which deepens by entrainment but shoals by reforming closer to the surface.

6. Summary

A coupled model consisting of an R30 atmospheric GCM connected to an ocean mixed layer model, is used to study variability of the upper ocean in the Northern Hemisphere. The ocean model consists of a grid of independent column models which allow for local air-sea energy exchange and the turbulent entrain-

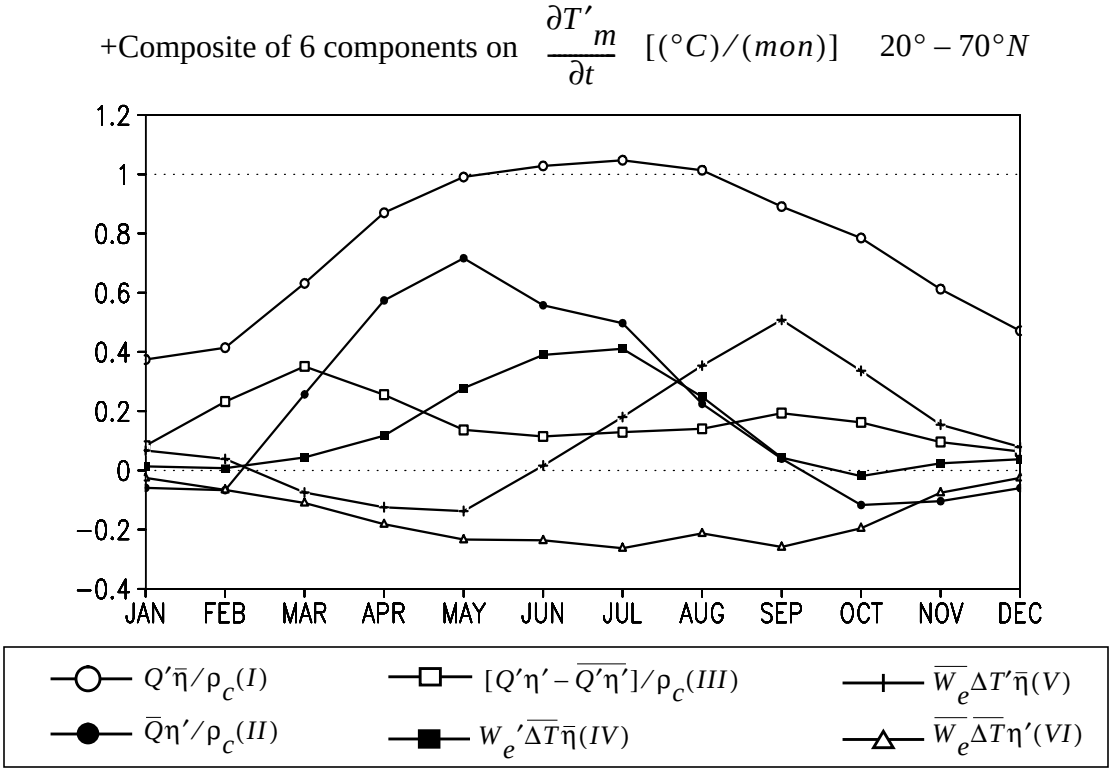

Fig. 11. Composite of the six leading components (˚C mon^{-1}) of the SST tendency equation (3) as a function of calendar month. The composites are constructed at each MLM grid point based on when the local monthly SST tendency exceeds one standard deviation, the resulting values are then averaged between 20˚N-70˚N.

ment of water into the surface mixed layer, but excludes currents and vertical motion. With the application of a seasonally varying surface flux correction, the long term monthly mean SSTs in a 50-year integration of the coupled model remain close observations.

The model does a reasonable job of simulating SST variability in midlatitudes. Like observations, the interannual standard deviation (σ) of SST in the model is slightly higher in September than in March and varies between 0.4-1.2˚C over most of the northern oceans in both months. However, the model is clearly deficient in the Gulf Stream region and the eastern tropical Pacific where currents and vertical motion strongly influence SSTs, and in the eastern portion of the subtropics where the AGCM does not properly simulate stratiform clouds. The model slightly underestimates SST σ, and the regions of maximum variability are located at about 20˚N-30˚N, 10˚-15˚ south of their observed position. In an additional coupled model integration with observed SSTs specified in the tropical Pacific, the simulated SST σ maximum in the Pacific during March is located at ~35˚N in agreement with observations, suggesting that SST variability in the central and eastern North Pacific during winter is dependent on ENSO.

The model simulates the general structure of the mean mixed layer depth ($\bar{h}$) north of 10˚S in both March and September well, but underestimates its magnitude in the North Atlantic during winter. As discussed in section 3, there are many reasons why *h* might be too small in the subpolar gyre of the North Atlantic in winter; analyses of ocean GCMs could help to elucidate the influence of currents on vertical shear and stratification and thus *h*. The regions of greatest mixed layer depth variability coincide with the maximum $\bar{h}$ in both winter and summer.

The surface and entrainment heat fluxes are the dominant terms in the SST tendency equation. The net surface heat flux strongly influences the mean seasonal cycle of SSTs and the development of SST anomalies throughout the year, but is especially dominant in winter. Entrainment of subsurface water into the mixed layer acts to cool SSTs over most of the Northern Hemisphere, except at high latitudes in the North Atlantic in winter and in portions of the tropical Pacific where the water is warmer at depth and salinity controls the density profile. Entrainment strongly influences SSTs anomalies in fall, especially north of ~35˚N (45˚N) in the Pacific (Atlantic). The impact of entrainment on SST tendencies depends mainly on the anomalous entrainment ($W'_e\overline{\Delta T}h$) in summer and the anomalous temperature jump at the base of the mixed layer $\overline{W_e}\Delta T'\bar{h}$ in fall. Anomalous entrainment also influences SSTs indirectly through the mixed layer depth, and *h'* has a significant impact on the SST' tendency during spring and summer. In agreement with Alexander and Penland [1996], the results of the present study suggest that while a fixed slab representation of the upper ocean may be reasonable in winter, changes in *h* and the heat flux through the base of the mixed layer play an important role in the development of SST anomalies during the remainder of the year.

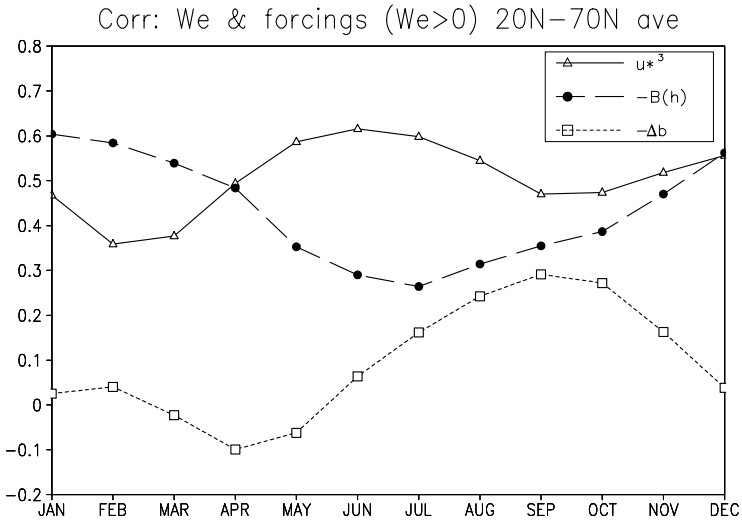

Fig. 12. Correlations of the entrainment rate (W_e) with the friction velocity (u_*^3), and the negative buoyancy forcing integrated over the mixed layer (-*B(h)*), and buoyancy jump at the base of the mixed layer (-Δ*b*) computed using daily anomalies within a given calendar month.

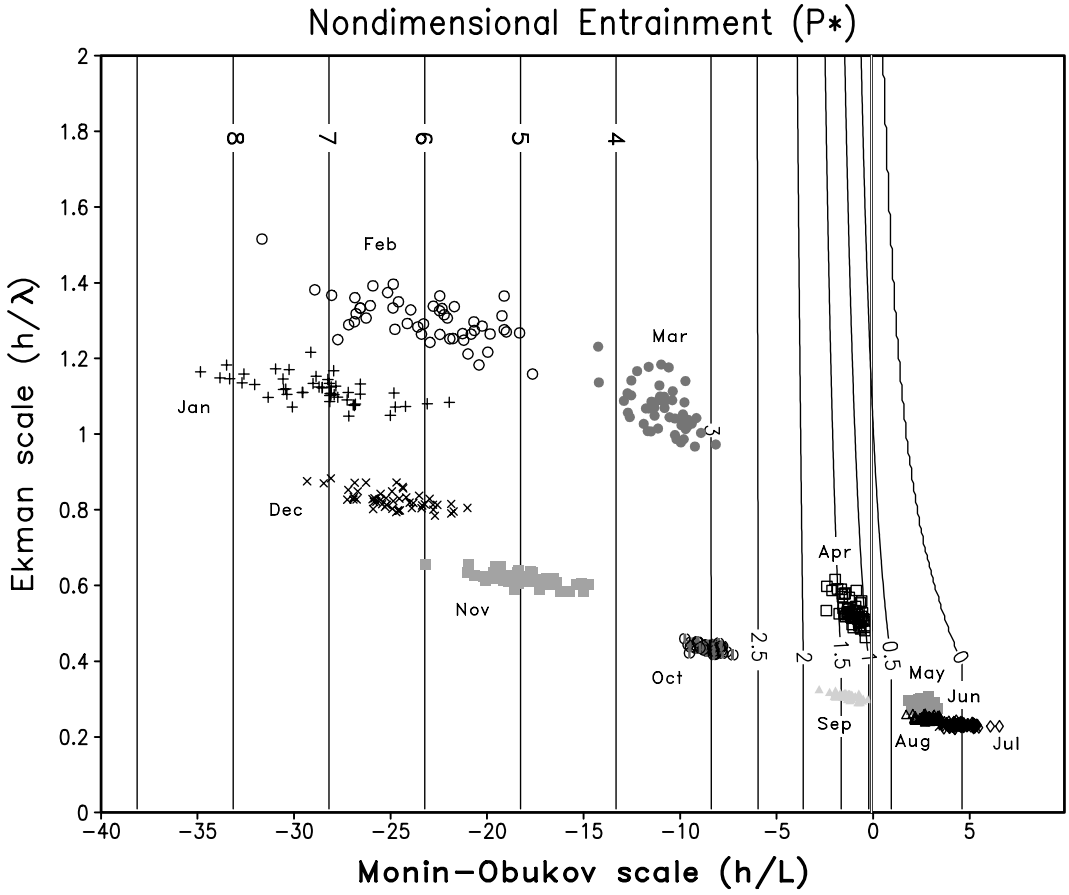

Fig 13. Non-dimensional mixing efficiency (P^*) as a function of the non-dimensional stability (h/L) and rotational (h/λ) parameters, which uniquely govern P^* in the MLM. The contour interval is 0.5 for 0.0 P^* 3.0 and 1.0 for P^*>3.0. Overlaid on the P^* contours is a scatter plot of h/L , h/λ obtained from the coupled model simulation, where h/L and h/λ are monthly means that have been averaged between 20˚N-70˚N.

Correlations between monthly anomalies of W_e and u_*^3, $B(h)$ and Δb indicate that wind mixing is the dominant term driving anomalous entrainment in summer, buoyancy forcing is most important in winter, while the density jump at the base of the mixed layer is of secondary importance throughout the year. However, the mechanical and buoyancy forcings are linked through their mutual dependence on the wind speed. Entrainment in the mixed layer model used here is governed by the Monin-Obukov ($u_*^3/B(h)$) and Rossby rotation (u_*/f) length scales. The former is dominant in the coupled model simulation especially in winter, although rotation can be important for determining whether shoaling occurs at any given time.

In this paper, we have focused on how surface fluxes and entrainment influences SST and mixed layer depth. Barsugli [1995] and Blade [1997] compared the behavior of a low resolution atmospheric model coupled to a 50 m slab ocean to an atmospheric simulation with specified SSTs assuming perpetual January conditions. These studies along with the idealized modeling study of Barsugli and Battisti [1997] found that midlatitude air-sea coupling leads to a reduction in thermal damping which results in an increase in the variance of the near surface air temperature and a slight enhancement of the persistence of certain atmospheric structures. Bhatt et al. [1998] confirmed the reduction of thermal damping in a coupled model which included the seasonal cycle and a variable depth mixed layer ocean model, but found that the subsurface storage of thermal anomalies and their re-entrainment into the mixed layer had an even greater impact on near surface air temperature variability on interannual time scales. In the future, we plan to compare the coupled model described here to an atmospheric GCM simulation in which the SSTs are specified to follow the long term mean seasonal cycle of the coupled run to study how midlatitude air-sea interaction

and mixed layer physics influence atmospheric variability.

Acknowledgements

We thank Gabriel Lau, Isaac Held, John Lanzante and Mary Jo Nath for providing to us the GFDL AGCM and model fields from the simulation with observed SSTs in the tropical Pacific as part of the GFDL-University Consortium project. Steve Worley at NCAR provided the observed mixed layer depth data. We also thank Joe Barsugli and Matt Newman for their valuable suggestions. This research was supported by NSF grant OCE95-31870 and NOAA grant GC98-139.

References

Alexander, M.A., Midlatitude atmosphere-ocean interaction during El Niño. Part I: the North Pacific Ocean, *J. Climate*, **5**, 944-958., 1992.

Alexander, M.A., and C. Deser, A mechanism for the recurrence of wintertime midlatitude SST anomalies, *J. Phys. Oceanogr.*, **25**, 122-137, 1995.

Alexander, M.A., and J. D. Scott, Web-based atlas of climatology and variability in the GFDL R30S14 GCM., [*Available on-line from http://www.cdc.noaa.gov/gfdl/*], 1999.

Alexander, M.A., and C. Penland, Variability in a mixed layer model of the upper ocean driven by stochastic atmospheric surface fluxes, *J. Climate*, **9**, 2424-2442, 1996.

Alexander, M.A., and J.D. Scott, Surface flux variability over the North Pacific and North Atlantic Oceans, *J. Climate*, **10** (11), 2963-2978, 1997.

Barsugli, J.J., Idealized models of intrinsic midlatitude atmosphere-ocean interaction., Ph.D. thesis, University of Washington, [*Available on line from http://www.cdc.noaa.gov/~jjb/thesis.html.*], 1995.

Barsugli, J.J., and D.S. Battisti, The basic effects of atmosphere-ocean thermal coupling on midlatitude variability., *J. Atmos. Sci.*, **55** (4), 477-493, 1998.

Battisti, D.S., U. S. Bhatt, and M.A. Alexander, A modeling study of the interannual variability in the wintertime North Atlantic Ocean, *J. Climate*, **8** (12), 3067-3083., 1995.

Bhatt, U.S., M. A. Alexander, D. S. Battisti, D. D. Houghton, and L.M. Keller, Atmosphere-ocean interaction in the North Atlantic: near-surface climate variability, *J. Climate*, **11**, 1615-1632, 1998.

Bjerknes, J., Atlantic air-sea interaction, *Adv. in Geophys*, **20**, 1-82, 1964.

Blade, I., The influence of midlatitude coupling on the low frequency variability of a GCM. Part I: No tropical SST forcing, *J. Climate*, **10**, 2087-2106, 1997.

Camp, N.T., and R.L. Elsberry, Oceanic thermal response to strong atmospheric forcing, II, the role of one-dimensional processes, *J. Phys. Oceanogr.*, **8**, 215-224, 1978.

Cayan, D.R., Latent and sensible heat flux anomalies over the northern oceans: driving the sea surface temperature, *J. Phys. Oceanogr.*, **22**, 859-881, 1992.

Clark, N.E., Specification of sea surface temperature anomaly patterns in the eastern North Pacific, *J. Phys. Oceanogr.*, **2**, 391-404, 1972.

Davis, R.E., R. Deszoeke, D. Halpern, and P. Niiler, Variability in the upper ocean during MILE. Part I: The heat and momentum balances, *Deep Sea Research*, **28**, 1427-1451, 1981.

Delworth, T., North Atlantic interannual variability in a coupled ocean-atmosphere model, *J. Climate*, **9** (10), 2356-2375, 1996.

Deser, C., and M.S. Timlin, Atmosphere-Ocean interaction on weekly time scales in the North Atlantic and Pacific, *J. Climate*, **10** (3), 393-408, 1997.

Dickson, R.R., J.R.N. Lazier, J. Meincke, P.B. Rhines, and J. Swift, Long-term coordinated changes in the convective activity of the North Atlantic, *Progress in Oceanography*, **38**, 241-295, 1996.

Elsberry, R.L., and R.W. Garwood, Numerical ocean prediction models-goal for the 1980s, *Bull. Amer. Meteor. Soc*, **61**, 1556-1566, 1980.

Favorite, F., and D.R. McLain, Coherence in transpacific movements of positive and negative anomalies of sea surface temperature, 1953-1960, *Nature*, **244**, 139-143, 1973.

Frankignoul, C., Sea surface temperature anomalies,

planetary waves, and air-sea feedback in the middle latitudes, *Rev. Geophys*., **23**, 357-390, 1985.

Frankignoul, C., and R.W. Reynolds, Testing a dynamical model for mid-latitude sea surface temperature anomalies, *J. Phys. Oceanogr.*, **13**, 1131-1145, 1983.

Garrat, J.R., A.J. Pratta, L.D. Rotstayn, and S. Cusack, The surface radiation budget over oceans and continents, *J. Climate*, **11**, 1951-1968, 1998.

Garwood, R.W., An oceanic mixed layer model capable of simulating cyclic states, *J. Phys. Ocean.*, **7**, 455-468, 1977.

Gascard, J.-C., and R.A. Clarke, The Formation of Labrador Sea Water. Part II: Mesoscale and smaller processes, *J. Phys. Oceanogr.*, **13**, 1779--1797, 1983.

Gaspar, P., Modeling the seasonal cycle of the upper ocean, *J. Phys. Ocean*, **18**, 161-180, 1988.

Gaspar, P., Y. Gregoris, R. Stull, and C. Boisser, Long-term simulations of upper ocean vertical mixing using models of different types., in Small-scale turbulence and mixing in the ocean, edited by N.J.C.J.a.B.M. Jamart, pp. 169-184, Elseveir, Amsterdam, 1988.

Gill, A.E., and P.P. Niiler, The theory of the seasonal variability in the ocean, Deep Sea Res., 20, 141-177, 1973.

Gill, A.E., and J.S. Turner, A comparison of seasonal thermocline models with observations, *Deep-Sea Res.*, **23**, 391-401, 1976.

Gordon, C., and M. Bottomley, The parameterization of the upper ocean mixed layer in coupled ocean-atmosphere models, in Coupled Ocean-Atmosphere Models, edited by J.C.J. Nihoul, pp. 613-635, Elsevier Oceanography series, New York, 1985.

Gordon, C.T., and W. Stern, A description of the GFDL global spectral model, *Mon. Wea. Rev.*, **110**, 625-644, 1982.

Halliwell, G.R., and D.A. Mayer, Frequency response properties of forced climatic SST anomaly variability in the North Atlantic, *J. Climate*, **9** (12, Part III), 3575-3587, 1996.

Haney, L.R., B.H. Houtman, and W.H. Little, The relationship between wind and sea surface temperature anomalies in the mid-latitude North Pacific Ocean, *Atmos. Ocean*, **21**, 168-186, 1983.

Haney, R.L., A numerical case study of the development of large-scale thermal anomalies in the central North Pacific Ocean, *J. Phys. Oceanogr.*, **10**, 541-556, 1980.

Hanson, H.P., COADS as a diagnostic modeling tool: air-sea interaction and the role of the deep ocean circulation in climate change, in Proceedings of the International COADS Workshop, edited by K.W. Henry Diaz, Scott Woodruff, pp. 315-322, NOAA, Boulder, CO, 1992.

Horel, J.D., and J.M. Wallace, Planetary-scale atmospheric phenomena associated with the interannual variability of sea surface temperature in the equatorial Pacific, *Mon. Wea. Rev.,* **109**, 813-829, 1981.

Hsuing, J., Estimates of global oceanic meridional heat transport, *J. Phys. Oceanogr.*, **15**, 1405-1413, 1985.

Iwasaka, N., and J.M. Wallace, Large scale air sea interaction in the Northern Hemisphere from a view point of variations of surface heat flux by SVD analysis., *J. Meteor. Soc. Japan*, **73** (4), 781-794, 1995.

Jacob, W.J., Numerical semiprediction of monthly mean sea surface temperature, *J. Geophys. Res.*, **72**, 1681-1689, 1967.

Kantha, L.H., and C.A. Clayson, An improved mixed layer model for geophysical applications, *J. Geophys Res.*, **99** (c12), 25235-25266, 1994.

Kim, J., A generalized bulk model of the oceanic mixed layer, *J. Phys.Oceanogr.*, **6**, 686-695, 1976.

Kraus, E.B., Merits and deffects of different approaches to mixed layer modelling, in Small-scale turbulence and mixing in the ocean, edited by N.J.C.J.a.B.M. Jamart, pp. 37-50, Elsevier, Amsterdam, 1988.

Kumar, A., and M.P. Hoerling, Annual cycle of Pacific North America seasonal predictability associated with different phases of ENSO., *J. Climate,* **11**, 3295-3308, 1998.

Lanzante, J.R., and R.P. Harnack, An investigation of summer sea surface temperature anomalies in the eastern North Pacific Ocean, *Tellus*, **35A**, 256-268, 1983.

Large, W.C., J.C. McWilliams, and S.C. Doney, Oceanic vertical mixing: a review and a model with a non-local boundary layer parameterization, ***Rev. Geophys***., 32, 363-404, 1994.

Large, W.G., J.C. McWilliams, and P.P. Niiler, Upper ocean thermal response to strong autumnal forcing over the Northeast Pacific, *J. Phys. Oceanogr.*, **16**, 1524-1550, 1986.

Lau, N.-C., and M.J. Nath, The role of the 'atmospheric bridge' in linking tropical Pacific ENSO events to extratropical SST anomalies., *J. Climate*, **9** (9), 2036-2057, 1996.

Le Treut, H., J.Y. Simonot, and M. Crepon, A model for the sea-surface temperature and heat content in the North Atlantic Ocean, in Coupled Ocean-Atmosphere Models, edited by J.C.J. Nihoul, pp. 439-446, Elsevier, Amsterdam, 1985.

Ledwell, J.R., A.J. Wilson, and C.S. Low, Evidence for slow mixing across the pychnocline from an open-ocean tracer release experiment, *Nature*, **364**, 701-703, 1993.

Luksch, U., Simulation of North Atlantic low frequency variability., *J. Climate*, **9** (9), 2083-2092, 1996.

Luksch, U., and H.v. Storch, Modeling the low-frequency sea surface temperature variability in the North Pacific, *J. Climate*, **5**, 893-906, 1992.

Manabe, S., and D.G. Hahn, Simulation of atmospheric variability, *Mon. Wea. Rev.*, **109**, 2260-2286., 1981.

Manabe, S., and R.J. Stouffer, Two stable equilibria of a coupled ocean-atmosphere model, *J. Climate*, **1**, 841-866, 1988.

Martin, P.J., Simulation of the mixed layers at OWS November and Papa with several models, J. *Geophys. Res.*, **90**, 903-916, 1985.

Miller, A.J., D.R. Cayan, T.P. Barnett, N.E. Graham, and J.M. Oberhuber, Interdecadal variability of the Pacific Ocean: model response to observed heat flux and wind stress anomalies, *Climate Dyn*., **10**, 287-302, 1994.

Mitchell, T.P., and J.M. Wallace, ENSO seasonality :1950-78 versus 1979-92., *J. Climate*, **9**, 3149-3161, 1996.

Miyakoda, K., and A. Rosatil, The variation of sea surface temperature in 1976 and 1977 2. The simulation with mixed layer models, *J. Geophys. Res.*, **89**, 6533-6542, 1984.

Moisan, J.R., and P.P. Niiler, The seasonal heat budget of the North Pacific: net heat flux and heat storage rates (1950-1990), *J. Phys. Oceanogr.*, **28** (3), 401-421, 1998.

Namais, J., Macroscopic association between mean monthly sea surface temperature and the overlying winds, *J. Geophys. Res.*, **70**, 2307-2318, 1965.

Namias, J., Recent seasonal interactions between North Pacific waters and the overlying atmospheric circulation, *J. Geophys. Res.*, **64**, 631-646, 1959.

Namias, J., Large-scale air-sea interactions over the North Pacific from summer (1962) through the subsequent winter, *J. Geophys. Res.*, **68**, 6171-6186, 1963.

Namias, J., Experiments in objectively predicting some atmospheric and oceanic variables for the winter of 1971-1972, *J. Appl. Meteor.*, **11**, 1164-1174, 1972.

Namias, J., and R.M. Born, Temporal coherence in North Pacific sea-surface temperature patterns, J. *Geophys*. Res., **75**, 5952-5955, 1970.

Namias, J., and R.M. Born, Further studies of temporal coherence in North Pacific sea surface temperatures, *J. Geophys. Res.*, **79**, 797-798, 1974.

Niiler, P.P., and E.B. Kraus, One dimension models of the upper ocean, in Modeling and Prediction of Upper Layers of the Ocean, edited by E.B. Kraus, pp. 143-172, Pergamon Press, 1977.

Norris, J.R., and C. Leovy, Interannual variability in stratiform cloudiness and sea surface temperature., *J. Climate*, **7**, 1915-1925., 1994.

Norris, J.R., Y. Zhang, and J.M. Wallace, Role of clouds in summertime atmosphere-ocean interactions over the North Pacific, *J. Climate*, **11**, 2482-2490,

1998.

Paulson, C., A., and J.J. Simpson, Irradience measurements in the upper ocean, *J. Phys. Oceanogr.*, **7**, 952-956, 1977.

Price, J.F., R.A. Weller, and R. Pinkel, Diurnal cycling: observations and models of the upper ocean response to diurnal heating, cooling, and wind mixing, *J. Geohpys. Res.*, **91** (c7), 8411-8427, 1986.

Salmon, R., and M.C. Hendershott, Large scale air-sea interactions with a simple general circulation model, *Tellus*, **28**, 228-242, 1976.

Sausen, R., K. Barthel, and K. Hasselmann, Coupled ocean-atmosphere models with flux correction, *Climate Dyn.*, **2**, 145-163, 1988.

Schneider, N., A. J. Miller, M.A. Alexander, and C. Deser, Subduction of decadal north Pacific temperature anomalies: observations and dynamics, *J. Phys. Oceanogr.*, **29**, in press, 1999.

Shinoda, T., and H.H. Hendon, Mixed layer modeling of intraseasonal variability in the tropical west Pacific, *J. CLimate*, **11** (10), 2668-2685, 1998.

Simonot, J.Y., H.L. Treut, and M. Crepon, A thermodynamic model of the global sea-surface temperature and mixed layer depth, in Small-Scale Turbulence and Mixing in the Ocean, edited by J.C.J. Nihoul, and B.M. Jamart, pp. 123-139, Elsevier, New York, 1988.

Smith, T.M., R.W. Reynolds, R.E. Livezey, and D.C. Stokes, Reconstruction of historical sea surface temperatures using empiracal orthogonal functions., *J. Climate*, **9**, 1403-1420, 1996.

Webster, P.J., and R. Lukas, TOGA COARE: the Coupled Ocean-Atmosphere Response Experiment, *Bull. Amer. Met. Soc.*, **73** (9), 1377-1416, 1992.

White, W., B., R. Bernstein, G. McNally, S. Pazan, and R. Dickson, The thermocline response to transient atmospheric forcing in the interior midlatitude North Pacific 1976-1978, *J. Phys. Oceanogr.*, **10**, 372-384, 1980.

Wilkin, J.L., J.V. Mansbridge, and J.S. Godfrey, Pacific Ocean heat transport at 24 degrees N in a high-resolution global model, *J. Phys. Oceanogr.*, **25** (10), 2204-2214.

Yu, L., and P. Malanotte-Rizzoli, Inverse modeling of seasonal variations in the North Atlantic Ocean, *J. Phys. Oceanogr.*, **28** (5), 902-922, 1998.